

Can SSD-Mamba2 Unlock Reinforcement Learning for End-to-End Motion Control?

Gavin Tao, Yinuo Wang*, and Jinzhao Zhou

Abstract—End-to-end reinforcement learning for motion control promises unified perception–action policies that scale across embodiments and tasks, yet most deployed controllers are either *blind* (proprioception-only) or rely on fusion backbones with unfavorable compute–memory trade-offs. Recurrent controllers struggle with long-horizon credit assignment, and Transformer-based fusion incurs quadratic cost in token length, limiting temporal and spatial context. We present a vision-driven cross-modal RL framework built on *SSD-Mamba2*, a selective state-space backbone that applies *state-space duality* (SSD) to enable both recurrent and convolutional scanning with hardware-aware streaming and near-linear scaling. Proprioceptive states and exteroceptive observations (e.g., depth tokens) are encoded into compact tokens and fused by stacked *SSD-Mamba2* layers. The selective state-space updates retain long-range dependencies with markedly lower latency and memory use than quadratic self-attention, enabling longer look-ahead, higher token resolution, and stable training under limited compute. Policies are trained end-to-end under curricula that randomize terrain and appearance and progressively increase scene complexity. A compact, state-centric reward balances task progress, energy efficiency, and safety. Across diverse motion-control scenarios, our approach consistently surpasses strong state-of-the-art baselines in return, safety (collisions and falls), and sample efficiency, while converging faster at the same compute budget. These results suggest that *SSD-Mamba2* provides a practical fusion backbone for scalable, foresighted, and efficient end-to-end motion control.

Index Terms—Artificial Intelligence, Machine Vision, Learning Systems, Road Vehicles, Cognitive Science

I. INTRODUCTION

QUADRUPEDAL robots are increasingly deployed in domains where safe and reliable mobility is critical, including inspection, disaster response, and exploration of unstructured terrains [1]. Unlike wheeled platforms, they can traverse rubble, stairs, and deformable substrates, but their control remains a longstanding challenge: locomotion must be robust under diverse dynamics, foresighted to anticipate hazards, and computationally efficient for deployment on embedded hardware [2].

Deep reinforcement learning (DRL) offers a promising route toward such capabilities by training policies end-to-end from interaction. While DRL has enabled agile behaviors across terrains and disturbances, most prior controllers fall short in one of two ways. Proprioception-only (“blind”) agents can maintain stability but lack foresight, reacting only after contact with obstacles [3]. In contrast, cross-modal approaches that fuse vision with proprioception provide anticipatory information but rely on backbones with unfavorable compute–memory

trade-offs [4]. Recurrent models struggle to capture long-horizon dependencies [5], hierarchical schemes complicate optimization [6], and Transformers incur quadratic costs in token length, limiting their ability to scale [7].

These limitations raise a broader question: *Can recent advances in sequence modeling unlock practical end-to-end RL for motion control?* To answer this, we explore the State Space Duality (SSD) formulation of Mamba2 [8], a selective state-space architecture that achieves near-linear time and memory complexity while retaining the ability to model long-range dependencies. Unlike attention-based fusion, *SSD-Mamba2* performs hardware-aware recurrent scanning, providing scalability without sacrificing foresight. This property makes it a compelling candidate for quadrupedal locomotion, where policies must integrate both proprioceptive states and depth observations in real time.

In this paper, we introduce a vision-driven cross-modal RL framework built on *SSD-Mamba2*. Proprioceptive states are embedded by a lightweight multilayer perceptron (MLP) [9], depth images are patchified into spatial tokens by a compact convolutional neural network (CNN) [10], and the resulting token sequence is fused by stacked *SSD-Mamba2* layers. Policies and value functions are then trained end-to-end with Proximal Policy Optimization (PPO) [11] under domain randomization and an obstacle-density curriculum. A compact state-centric reward further encourages progress, energy efficiency, and safety [12].

The main contributions of this paper are summarized as follows:

- 1) **Establishing SSD-Mamba2 as a backbone for RL motion control.** We present the first work to leverage the SSD-based Mamba2 architecture in RL for end-to-end motion control, demonstrating its suitability as an efficient and scalable sequence model in this domain.
- 2) **Demonstrating effective cross-modal fusion.** We show that *SSD-Mamba2* provides an efficient and expressive backbone for integrating proprioceptive states with depth-image tokens. Its near-linear scaling, stable recurrent updates, and ability to capture long-range dependencies enable foresighted and robust control, outperforming Transformer-based and proprioception-only approaches.
- 3) **Validating end-to-end training with PPO.** We integrate *SSD-Mamba2* into a PPO pipeline, complemented by domain randomization, obstacle-density curricula, and a compact state-centric reward. This design yields faster convergence, higher training efficiency, and more

Corresponding author: Yinuo Wang.

stable performance than established baselines.

4) **Comprehensive empirical evaluation.** Through extensive experiments across diverse motion-control tasks, we demonstrate that SSD-Mamba2 improves performance, reduces collisions and falls, and generalizes better than state-of-the-art methods, supporting its potential for safety-critical robotic applications.

The remainder of this paper is organized as follows. Section II reviews related work on blind and cross-modal locomotion. Section III presents the methodology, including the problem formulation, the SSD-Mamba2 fusion backbone, and PPO optimization. Section IV describes the experimental setup and reports results, ablations, and analyses of efficiency, stability, and generalization. Section V concludes the paper and discusses future research directions.

II. RELATED WORK

A. Quadrupedal Locomotion Control

Research on quadrupedal locomotion has traditionally followed two paradigms: model-based control and learning-based methods. Early rule-based approaches relied on template dynamics, heuristics, and hand-engineered gait patterns for balance and foot placement [13]–[16], providing insights into leg coordination but limited adaptability to diverse environments. Later, model-based pipelines advanced to constrained optimal control, including trajectory optimization over centroidal or full-body dynamics and model predictive control (MPC) with explicit contact constraints and task hierarchies [17]–[20]. These methods achieved robust disturbance rejection and stable locomotion in structured settings, with examples such as MPC-based whole-body controllers for stair climbing and rapid trotting [21]–[23]. However, such controllers require accurate models of dynamics, ground contact, and friction, along with significant manual cost tuning. This reliance limits their scalability to unstructured or rapidly changing terrains, such as rubble or deformable substrates.

By contrast, learning-based methods aim to reduce modeling effort by training adaptive policies directly from interaction. Model-free deep reinforcement learning (DRL) in particular has shown strong potential for quadrupeds in diverse scenarios [24]–[26]. With large-scale domain randomization, policies trained in simulation have been successfully transferred to hardware [27], [28]. Recent work has further improved adaptability, such as rapid motor adaptation (RMA) [29], which augments a base policy with an adaptation module to handle payload changes and novel terrains online. DRL policies have also demonstrated robustness under water, mud, and snow conditions [30], [31]. Despite these advances, the majority of policies remain proprioception-only. Blind controllers can recover from disturbances but lack foresight and react only after contact events [3], which limits proactive obstacle avoidance and foothold planning. This motivates incorporating exteroceptive sensing such as vision to endow quadrupeds with anticipatory capability.

B. Vision-Driven Reinforcement Learning

Vision has emerged as a powerful complement to proprioception by providing spatial foresight. Visual information

enables robots to perceive obstacles before contact, anticipate irregular terrain, and plan footholds or body trajectories proactively. Several studies have incorporated visual input directly into DRL pipelines. For instance, [?] showed that depth-augmented RL policies could traverse rough terrain with greater robustness than proprioceptive baselines. [?] combined heightmap observations with a depth-to-heightmap predictor, enabling sim-to-real transfer on hardware. ViTAL [32] used vision for terrain-aware foothold selection and pose adaptation, improving safety on irregular surfaces. Other works explored semantic segmentation or heightmap predictors to enhance terrain awareness [4]. Hierarchical designs [6] further decomposed vision-based locomotion into high-level planning and low-level control.

However, fusion strategies for vision and proprioception present trade-offs. Simple feature concatenation underuses spatial structure and temporal dependencies, leading to limited generalization. Hierarchical formulations complicate optimization and can propagate errors across levels. Transformer-based fusion improves foresight but incurs quadratic time and memory scaling in token length, limiting input resolution and training efficiency [7], [33]. As a result, despite their promise, many vision-driven RL frameworks remain difficult to scale or deploy efficiently. This motivates the search for backbones that retain foresight while being more computationally tractable.

C. Sequence Models for Cross-Modal Fusion

A central challenge in vision-driven RL is the design of effective cross-modal fusion backbones. Recurrent neural network (RNN)-based approaches, such as long short-term memory (LSTM) and gated recurrent unit (GRU) architectures, have been used to integrate visual and proprioceptive information for quadrupedal locomotion [34], [35]. These methods capture temporal context but suffer from vanishing gradients and limited long-horizon memory, especially in extended locomotion sequences. Transformer-based models have recently become popular for cross-modal fusion [7], offering strong representational power and long-range context modeling. However, Transformers scale quadratically with sequence length, which constrains spatial resolution, temporal context, and training efficiency. This makes them costly for real-time quadrupedal control, where compute and memory budgets are limited.

State-space models (SSMs) offer an alternative by updating compact recurrent states with near-linear complexity [36]. The S4 model [37] first demonstrated efficient long-range dependency modeling on long-sequence benchmarks. Building on this, Mamba [38] introduced selective state updates with hardware-aware parallel scanning, achieving linear-time sequence modeling with strong throughput and memory efficiency. Variants such as AlignMamba [39], FusionMamba [40], and DepMamba [41] have extended this paradigm to multimodal tasks, showing improvements in alignment, fusion, and cross-modal consistency. More recently, Mamba2 advanced this line of work through the SSD formulation, which further enhances stability and expressivity while retaining near-linear scaling [8]. SSD-Mamba2 combines the efficiency

of selective scanning with dual state representations, enabling more reliable modeling of long-horizon dependencies.

To the best of our knowledge, this is the first work to use cross-modal SSD-Mamba2 for quadrupedal locomotion.

III. METHODOLOGY

A. Overview

We propose an end-to-end reinforcement learning framework that employs the SSD-based Mamba2 architecture as a fusion backbone for quadrupedal motion control. The overall pipeline is illustrated in Fig. 1. At each time step, the agent receives both proprioceptive and visual observations. Proprioceptive states are embedded by a lightweight MLP, while depth images are patchified into spatial tokens by a compact CNN. These tokens are fused by stacked SSD-Mamba2 layers (Fig. 2) through hardware-aware selective scanning, which achieves near-linear time and memory scaling. This design preserves long-horizon dependencies while reducing latency and memory usage compared with quadratic self-attention. The recurrent formulation also accommodates variable token lengths and resolutions, enabling a broader perceptual context, while input-gated, exponentially decaying dynamics provide a stabilizing inductive bias. The fused representation is consumed by policy and value heads, which are optimized end-to-end using PPO. Training is further enhanced by domain randomization and an obstacle-density curriculum, which expand environmental diversity and progressively increase task difficulty. A compact state-centric reward encourages balanced policies that make forward progress efficiently and safely.

B. Problem Formulation

1) **Markov Decision Process:** The motion-control task is formulated as a Markov Decision Process (MDP) [33] $\mathcal{M} = (\mathcal{S}, \mathcal{A}, \mathcal{P}, r, \gamma)$, where \mathcal{S} is the state space, \mathcal{A} is the action space, $\mathcal{P}(s_{t+1} | s_t, a_t)$ is the transition distribution defined by the physics simulator, and $r(s_t, a_t)$ is the reward function. The goal is to learn a policy $\pi_\theta(a_t | s_t)$ that maximizes the expected discounted return:

$$J(\pi) = \mathbb{E}_\pi \left[\sum_{t=0}^{T-1} \gamma^t r(s_t, a_t) \right], \quad (1)$$

with discount factor $\gamma \in (0, 1)$.

2) **Observation space:** At each time step t , the agent receives a multimodal observation:

$$s_t = \left\{ s_t^{\text{prop}}, I_{t-3:t}^{\text{depth}} \right\}, \quad (2)$$

where $s_t^{\text{prop}} \in \mathbb{R}^{93}$ is a proprioceptive vector containing IMU readings, local joint rotations, and the actions executed in the previous three steps. The term $I_{t-3:t}^{\text{depth}} = \{I_{t-3}^{\text{depth}}, I_{t-2}^{\text{depth}}, I_{t-1}^{\text{depth}}, I_t^{\text{depth}}\}$ denotes a stack of four recent depth frames, each with resolution 64×64 .

3) **Action space:** The action $a_t \in \mathbb{R}^{12}$ specifies the desired joint position targets for the robot's 12 actuated joints. A proportional-derivative (PD) controller [42] converts these position targets into torque commands applied to the actuators.

4) **Reward function:** The reward encourages forward progress while discouraging unsafe or inefficient behaviors. It is defined as

$$R_t = \alpha_{\text{fwd}} R_t^{\text{fwd}} + \alpha_{\text{energy}} R_t^{\text{energy}} + \alpha_{\text{alive}} R_t^{\text{alive}} + K_t \cdot R_t^{\text{sphere}}, \quad (3)$$

with coefficients $\alpha_{\text{fwd}}=1$, $\alpha_{\text{energy}}=0.005$, and $\alpha_{\text{alive}}=0.1$.

The forward term rewards task-aligned locomotion,

$$R_t^{\text{fwd}} = \langle v_t, e_x \rangle, \quad (4)$$

where v_t is the base linear velocity and e_x is the unit vector along the desired direction. The energy term penalizes excessive control effort,

$$R_t^{\text{energy}} = -\|\tau_t\|_2^2, \quad (5)$$

where τ_t denotes realized joint torques.

The alive term R_t^{alive} encourages the agent to remain operational. It provides a constant reward of 1.0 at each time step until termination. Termination is triggered by dangerous behaviors such as falling down or colliding irrecoverably with obstacles.

The sphere collection reward R_t^{sphere} (whenever applicable) is added whenever the agent collects a sphere, where K_t denotes the number of spheres collected at the current time step.

This compact, state-centric reward balances task performance, efficiency, and safety, facilitating stable on-policy learning.

C. SSD-Mamba2 Fusion Backbone

The SSD-Mamba2 backbone integrates proprioceptive and visual observations into a unified representation for control. It extends SSMs with SSD, which equips the model with both a recurrent and a convolutional formulation, ensuring efficient long-horizon modeling with near-linear complexity. The backbone can be described in four components:

1) **Tokenization of multimodal inputs:** At each time step t , the proprioceptive state $s_t^{\text{prop}} \in \mathbb{R}^{D_p}$ is mapped into a token

$$z_t^{\text{prop}} = W_p f_{\text{MLP}}(s_t^{\text{prop}}), \quad z_t^{\text{prop}} \in \mathbb{R}^d, \quad (6)$$

while the depth image $I_t^{\text{depth}} \in \mathbb{R}^{H \times W}$ is patchified into N tokens

$$z_t^{\text{vis}} = W_v f_{\text{CNN}}(I_t^{\text{depth}}), \quad z_t^{\text{vis}} \in \mathbb{R}^{N \times d}. \quad (7)$$

The concatenated sequence is

$$U_t = [z_t^{\text{prop}}; z_t^{\text{vis}}] \in \mathbb{R}^{(1+N) \times d}. \quad (8)$$

2) **Selective state-space update:** For token $u_{t,k}$, each SSD-Mamba2 layer maintains a recurrent state $x_{t,k}$ and updates it with input-gated dynamics:

$$x_{t,k+1} = \sigma(W_A u_{t,k}) x_{t,k} + \sigma(W_B u_{t,k}) u_{t,k}, \quad (9)$$

$$y_{t,k} = \sigma(W_C u_{t,k}) x_{t,k} + \sigma(W_D u_{t,k}) u_{t,k}, \quad (10)$$

where $\sigma(\cdot)$ denotes elementwise gating functions. This recurrent formulation yields an implicit convolutional view,

$$y_{t,k} = \sum_{i=0}^k K_{k,i}(u_{t,.}) u_{t,k-i}, \quad (11)$$

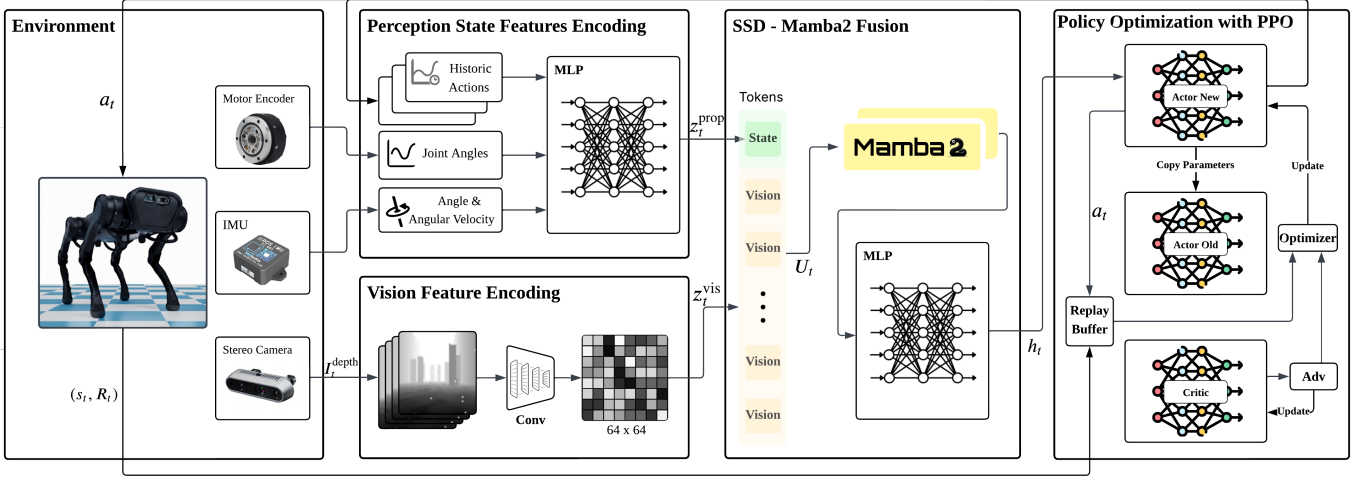


Fig. 1: Overall architecture of the proposed framework. Proprioception and depth are encoded into tokens by MLP/CNN, fused by a SSD-Mamba2 backbone, and optimized with PPO.

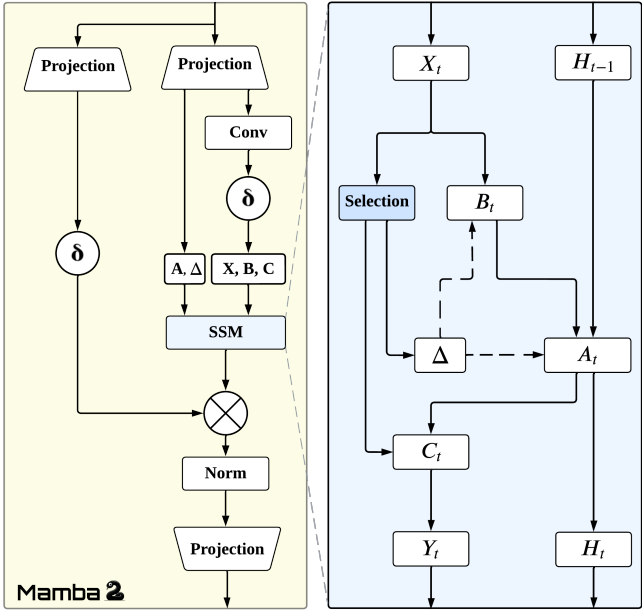


Fig. 2: Schematic of a Mamba2 SSM Layer.

with exponentially decaying coefficients $K_{k,i}$ that stabilize long-horizon modeling.

3) **Stacked backbone:** With L_m stacked layers, hidden states are refined with residual connections and normalization:

$$H_t^{(\ell+1)} = \text{LN}(Y_t^{(\ell)} + H_t^{(\ell)}), \quad \ell = 0, \dots, L_m - 1. \quad (12)$$

4) **Output representation:** The final representation aggregates spatial tokens and fuses them with the proprioceptive token:

$$\bar{y}_t^{\text{vis}} = \frac{1}{N} \sum_{i=1}^N y_t^{\text{vis}}, \quad h_t = f_{\text{head}}([y_t^{\text{prop}}; \bar{y}_t^{\text{vis}}]). \quad (13)$$

Remark 1. For quadrupedal motion control, SSD-Mamba2 confers three practical benefits. First, its near-linear scaling in tokens reduces the inference latency and memory foot-

print, which is critical for onboard deployment under real-time constraints. Second, the state-space duality formulation enables stable long-horizon dependency modeling, allowing the agent to anticipate terrain changes and obstacles beyond immediate sensor readings. Third, the input-gated dynamics provide robustness to sensor noise and varying image resolutions, mitigating performance degradation when proprioceptive or visual signals are imperfect. Together, these properties make SSD-Mamba2 a strong fusion backbone for safety-critical locomotion, where foresight, efficiency, and robustness are indispensable.

D. Policy Optimization with PPO

PPO is a widely used model-free reinforcement learning algorithm for continuous control due to its stability and simplicity. Instead of performing large, potentially destabilizing policy updates, PPO restricts the update step with a clipping mechanism, ensuring stable and efficient training [11]. The objective of PPO is defined as:

$$\pi^* = \arg \max_{\pi} \mathbb{E}_t \left[\min \left(\rho_t(\theta) \hat{A}_t, \text{clip}(\rho_t(\theta), 1-\epsilon, 1+\epsilon) \hat{A}_t \right) \right], \quad (14)$$

where π denotes the policy, \hat{A}_t is the estimated advantage at time t , and $\rho_t(\theta)$ is the importance sampling ratio:

$$\rho_t(\theta) = \frac{\pi_{\theta}(a_t | s_t)}{\pi_{\theta_{\text{old}}}(a_t | s_t)}. \quad (15)$$

The clipping parameter ϵ limits the range of policy updates, preventing large deviations from the previous policy.

The advantage \hat{A}_t is estimated via Generalized Advantage Estimation (GAE) to reduce variance:

$$\delta_t = r_t + \gamma V_{\phi}(s_{t+1}) - V_{\phi}(s_t), \quad \hat{A}_t = \sum_{l=0}^{T-t-1} (\gamma \lambda)^l \delta_{t+l}, \quad (16)$$

where γ is the discount factor and λ balances bias and variance.

The critic is trained to minimize the squared error between predicted and empirical returns:

$$\mathcal{L}_V(\phi) = \frac{1}{2} \mathbb{E}_t \left[(V_\phi(s_t) - \hat{R}_t)^2 \right], \quad (17)$$

where $\hat{R}_t = \sum_{k=t}^T \gamma^{k-t} r_k$ is the empirical return.

Finally, entropy regularization is added to encourage exploration:

$$\mathcal{H}_t = - \sum_a \pi_\theta(a | s_t) \log \pi_\theta(a | s_t). \quad (18)$$

The complete loss function for training both policy and value networks is:

$$\mathcal{J}(\theta, \phi) = -\mathcal{L}_{\text{clip}}(\theta) + \beta_V \mathcal{L}_V(\phi) - \beta_H \mathbb{E}[\mathcal{H}_t], \quad (19)$$

where β_V and β_H are coefficients for value loss and entropy regularization, respectively. By balancing policy improvement, value estimation, and exploration, PPO provides stable and efficient end-to-end training for our SSD-Mamba2 backbone.

Remark 2. While PPO provides stable on-policy updates, additional mechanisms are required to ensure robustness in complex locomotion tasks. We therefore incorporate *domain randomization*, which perturbs terrain friction, obstacle appearance, and sensor noise during training, and a *curriculum schedule*, which gradually increases obstacle density and terrain complexity. These strategies expose the agent to diverse conditions, mitigate overfitting to specific environments, and reduce catastrophic failures such as falls and collisions. As a result, SSD-Mamba2 policies not only converge faster but also generalize more reliably to unseen scenarios.

IV. EXPERIMENTS

A. Environment Setup

All experiments are carried out on a laptop with an Intel Xeon(R) Platinum 8358P CPU (128 cores, 2.6 GHz base frequency) and a NVIDIA GeForce RTX 3090 GPU (24 GB, CUDA 12.8). The computing environment is based on Ubuntu 22.04, with physics simulation executed in PyBullet [43]. All models are developed in Python 3.8 using PyTorch 2.4.1.

The model is evaluated across three simulated environments that vary in terrain difficulty and obstacle shapes:

- **Thin Obstacle with Goals:** flat terrain populated with numerous thin cuboid obstacles and goals that offering extra rewards .
- **Rugged Terrain with Obstacles and Goals:** uneven, discontinuous ground with a maximum height of 5 cm, same thin obstacles and goals settings as above, requiring careful placement of foothold.
- **Sphere Obstacles with Goals:** flat terrain with sphere-shaped obstacles that has the same shape as the goals.

Fig. 3 shows representative examples. Unless noted otherwise, obstacle layouts are randomized at episode reset; only *Dynamic Obstacle* updates obstacle positions during an episode.

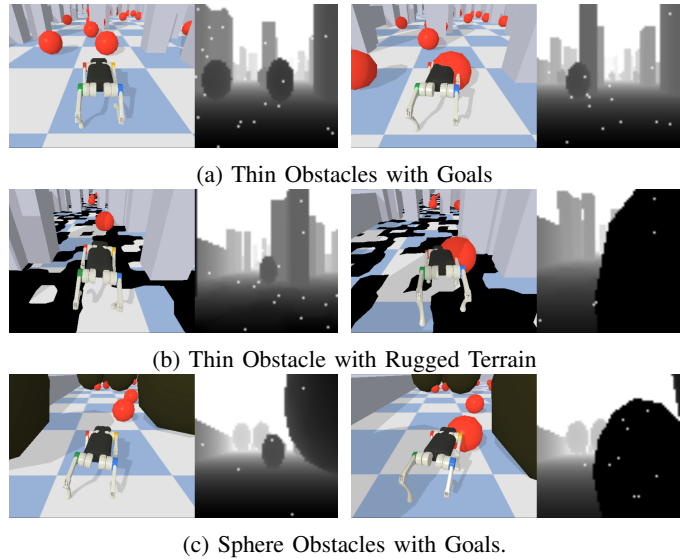


Fig. 3: Simulated environments. Obstacle layouts are randomized at reset; all obstacle positions are static during an episode.

B. Baseline Methods

To evaluate the effectiveness of the proposed framework, we compare against the following baselines:

- **Proprio-Only.** A blind agent that relies solely on the 84-dimensional proprioceptive vector, without any exteroceptive input.
- **Transformer Proprio-Vision.** A Transformer-based model that applies self-attention over visual tokens together with a proprioceptive token, representing attention-driven cross-modal fusion [7].
- **Transformer Vision-Only.** A Transformer-based model that uses depth tokens alone as input, following the same architecture as the Transformer Proprio-Vision baseline.
- **Mamba2 Vision-Only.** Using the depth observations alone as input and the same Mamba2-based encoder is used to process the vision tokens.

All baselines are trained with the same PPO algorithm, domain randomization strategy, and curriculum schedule, and are evaluated under identical experimental conditions. Where applicable, the same proprioceptive and depth encoders, along with the same token width, are reused to minimize confounding effects from differences in representation size.

C. Implementation Details

a) Model architecture.: As illustrated in Fig. 1, the network consists of lightweight encoders, an SSD-Mamba2 fusion backbone, and compact projection heads for policy and value estimation. The detailed architectural settings are summarized in Table I.

b) Training schema.: All policies are trained with PPO using on-policy rollouts of length T , minibatch updates over multiple epochs, advantage normalization, and gradient clipping. Terrain and appearance randomization are applied at episode resets, and an obstacle-density curriculum gradually increases task difficulty. The overall training procedure is

TABLE I: Network architecture settings.

Component	Configuration
Token width d	128
Proprio encoder	2-layer MLP (256, 256), ReLU
Visual token projection	CNN patchify \rightarrow linear to width d (≈ 128)
Mamba2 backbone	$L_m=2$ stacked SSD-Mamba2 layers, residual + LayerNorm
Projection head	2-layer MLP (256, 256), ReLU

TABLE II: PPO hyperparameters.

Hyperparameter	Value
Episode horizon (steps)	999
Samples per iteration	16,384
Minibatch size	1,024
Optimization epochs per update	3
Discount factor γ	0.99
GAE parameter λ	0.95
PPO clip parameter ϵ	0.2
Entropy coefficient	0.005
Policy learning rate	1×10^{-4}
Value learning rate	1×10^{-4}
Optimizer	Adam
Activation function	ReLU

outlined in Algorithm 1. Shared PPO hyperparameters are listed in Table II.

c) *Domain randomization*.: To improve robustness and transferability, physics parameters are randomized at the beginning of each episode [44]. Unless stated otherwise, the sampled values remain fixed throughout the episode. Table III lists the randomized ranges.

d) *Visual perturbations*.: To simulate sensor artifacts, light-weight noise is injected into depth observations. Specifically, $K \sim \mathcal{U}\{3, \dots, 30\}$ pixel locations are selected per frame and their values set to the maximum sensor range, producing salt-like saturation effects. This perturbation is applied consistently across all methods.

e) *Obstacle-density curriculum*.: In obstacle-rich environments, training begins with sparse obstacle placement and linearly increases density to the target distribution as learning progresses [45]. This schedule is applied identically to all compared methods.

D. Evaluation Metrics

The learned policies are assessed using three metrics. (i) *Mean episode return*, which summarizes overall task performance. (ii) *Distance moved*, defined as the displacement (in meters) achieved along the task-aligned target direction. (iii) *Collision times*, measured as the number of collisions recorded until either three evaluation episodes are completed or the robot falls. Collision checks are performed at every control step, and the collision metric is reported only in scenarios containing obstacles and only for episodes in which at least one collision occurs.

E. Experiment Results

1) **Performance vs. Baselines**: We benchmark *SSD-Mamba2* against four baselines in the *Thin Obstacle & Goals*

TABLE III: Domain randomization ranges.

Parameter	Range	Units
K_P	[40, 90]	-
K_D	[0.4, 0.8]	-
Link inertia	$[0.5, 1.5] \times$ default	-
Lateral friction	[0.5, 1.25]	N·s/m
Body mass	$[0.8, 1.2] \times$ default	kg
Motor friction	[0.0, 0.05]	N·m·s/rad
Motor strength	$[0.8, 1.2] \times$ default	N·m
Sensor latency	[0, 0.04]	s

Algorithm 1 SSD-Mamba2 End-to-End Training with PPO

Require: Policy parameters θ , value parameters ϕ , fusion module f_{fuse} , horizon T , PPO/GAE hyperparameters $(\gamma, \lambda, \epsilon, \beta_V, \beta_H)$, domain randomization ranges \mathcal{R} , curriculum scheduler \mathcal{C}

Ensure: Trained policy π_θ and value function V_ϕ

- 1: Initialize curriculum state $c \leftarrow \mathcal{C}.\text{INIT}()$
- 2: **for** iteration $k = 1, 2, \dots$ **do**
- 3: Sample environment appearance and obstacle density from \mathcal{C}
- 4: Initialize replay buffer $\mathcal{D} \leftarrow \emptyset$
- 5: **while** $|\mathcal{D}| < N_{\text{iter}}$ **do**
- 6: Sample physics params $\xi \sim \mathcal{R}$; reset environment
- 7: **for** $t = 1$ to T **do**
- 8: Observe $o_t = \{s_t^{\text{prop}}, I_{t-3:t}^{\text{depth}}\}$ and inject depth noise
- 9: Fuse tokens: $h_t \leftarrow f_{\text{fuse}}(o_t)$
- 10: Sample action $a_t \sim \pi_\theta(\cdot | h_t)$, step environment, obtain $(r_t, o_{t+1}, \text{done})$
- 11: Store $(h_t, a_t, r_t, \log \pi_\theta, V_\phi(h_t), \text{done})$ in \mathcal{D}
- 12: **if** done **then break**
- 13: **end if**
- 14: **end for**
- 15: **end while**
- 16: Compute advantages \hat{A}_t with GAE, normalize, and compute returns \hat{R}_t
- 17: **for** epoch = 1 to E **do**
- 18: **for** minibatch $\mathcal{B} \subset \mathcal{D}$ **do**
- 19: Compute ρ_t , clipped policy loss $\mathcal{L}_{\text{clip}}$, value loss \mathcal{L}_V , and entropy \mathcal{H}
- 20: Update (θ, ϕ) minimizing $-\mathcal{L}_{\text{clip}} + \beta_V \mathcal{L}_V - \beta_H \mathcal{H}$
- 21: **end for**
- 22: **end for**
- 23: Advance curriculum: $c \leftarrow \mathcal{C}.\text{ADVANCE}(c)$
- 24: **end for**

environment. Figure 4 shows training curves (mean \pm one standard deviation across 10 seeds), and Table IV reports final metrics.

From Fig. 4, *SSD-Mamba2* shows a steeper early slope, higher asymptotic return, and tighter confidence band than all baselines. Numerically (Table IV), *SSD-Mamba2* improves return over *Transformer Proprio-Vision* from 354.4 to 537.7 (+51.7%), reduces collisions from 202.5 to 193.7 (-4.3%), and

TABLE IV: Performance comparison in the *Thin Obstacle & Goals* environment. Mean \pm std over 10 runs.

Method	Return	Collision Times	Distance Moved (m)
Proprio-Only	56.34 \pm 33.37	571.16 \pm 148.41	3.29 \pm 0.97
Transformer Vision-Only	13.44 \pm 35.07	—	1.27 \pm 0.88
Mamba2 Vision-Only	16.75 \pm 38.22	—	1.54 \pm 1.04
Transformer Proprio-Vision	354.40 \pm 352.59	202.47 \pm 131.72	7.55 \pm 5.74
SSD-Mamba2 (Ours)	537.67 \pm 307.79	193.70 \pm 93.61	10.50 \pm 5.36

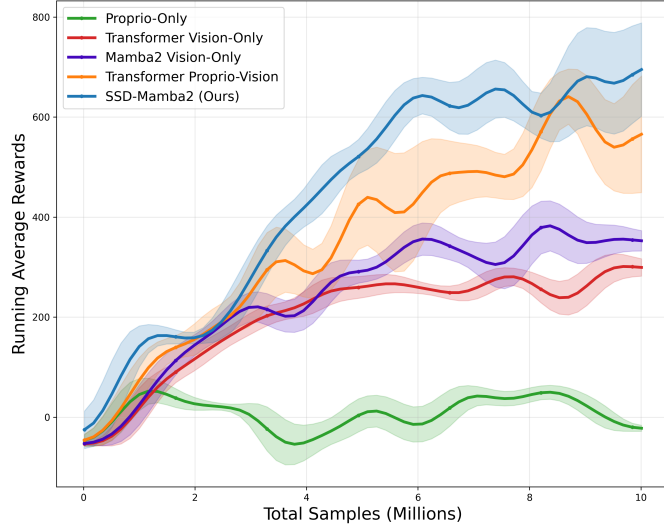


Fig. 4: Training learning curves on *Thin Obstacle & Goals*. Solid lines denote mean episode return across seeds; shaded regions indicate \pm one standard deviation.

increases distance from 7.55 m to 10.50 m (+39.1%). These results indicate both higher peak performance and more stable optimization.

2) **Ablation: Effect of Multi-Modality:** Single-modality agents perform poorly. *Proprio-Only* achieves a return of 56.3, with 571.2 collisions and only 3.29 m traveled. Vision-only agents barely progress: *Transformer Vision-Only* reaches a return of 13.4 with 1.27 m distance, while *Mamba2 Vision-Only* yields 16.8 return and 1.54 m distance.

Adding vision to proprioception provides substantial gains. *Transformer Proprio-Vision* improves over *Proprio-Only* by raising return from 56.3 to 354.4 (+529%), reducing collisions from 571.2 to 202.5 (-64.5%), and increasing distance from 3.29 m to 7.55 m (+129.5%). It also outperforms *Transformer Vision-Only*, achieving a return more than $25.4 \times$ higher (354.4 vs. 13.4) and a distance nearly $6 \times$ longer (7.55 m vs. 1.27 m), while providing meaningful collision reduction.

Our proposed *SSD-Mamba2* further amplifies these benefits. Compared with *Mamba2 Vision-Only*, it delivers over $30 \times$ higher return (537.7 vs. 16.8) and about $6.8 \times$ longer distance (10.50 m vs. 1.54 m). Relative to *Proprio-Only*, it boosts return nearly $9.5 \times$ (537.7 vs. 56.3) while cutting collisions by 66% (193.7 vs. 571.2).

These results confirm that multi-modality is essential for foresighted locomotion.

3) **Ablation: Effect of the Fusion Backbone:** Among vision-only agents, *Mamba2 Vision-Only* provides modest

gains over *Transformer Vision-Only*, improving return from 13.4 to 16.8 (+25.4%) and distance from 1.27 m to 1.54 m (+21.3%). However, both remain far from the performance of multi-modal agents.

For multi-modal inputs, *SSD-Mamba2* outperforms *Transformer Proprio-Vision*, increasing return from 354.4 to 537.7 (+51.7%), raising distance from 7.55 m to 10.50 m (+39.1%), and slightly lowering collisions from 202.5 to 193.7 (-4.3%).

Overall, the backbone choice becomes decisive once multi-modal inputs are available: *SSD-Mamba2* delivers more effective fusion and superior control outcomes than attention-based fusion under the same training protocol.

4) **Generalization to Unseen Conditions:** A central challenge for quadrupedal controllers is whether policies trained in one environment can transfer to unseen conditions without fine-tuning. We therefore train all agents in *Thin Obstacle & Goals* and evaluate them zero-shot in two novel scenarios: *Rugged Terrain with Thin Obstacles & Goals* and *Sphere Obstacles & Goals*. These settings introduce irregular surfaces and altered obstacle geometry, testing the robustness and foresight of the learned policies.

Rugged terrain (Table V): On uneven surfaces, proprioception alone is insufficient, yielding only 70.2 return and 3.44 m distance. Adding vision improves foresight: *Transformer Proprio-Vision* reaches 432.3 return and 9.22 m distance, demonstrating the benefit of multi-modal fusion. *SSD-Mamba2* further improves return to 601.6 (+39.2%) and distance to 11.31 m (+22.7%) over *Transformer Proprio-Vision*, while keeping collisions competitive (638.9 vs. 560.5). The slightly higher collision rate (+14.0%) suggests that our policy explores more aggressively to achieve longer progress on rugged ground. Overall, *SSD-Mamba2* attains the best performance in return and distance, underscoring the resilience of selective state-space fusion.

Sphere obstacles (Table VI): With spherical hazards, single-modality agents again fail to progress meaningfully, moving less than 6 m on average. *Transformer Proprio-Vision* improves substantially (467.6 return, 10.26 m distance, 163.2 collisions). *SSD-Mamba2* surpasses it with 608.5 return (+30.1%), 12.24 m distance (+19.3%), and slightly fewer collisions (158.8, -2.7%). This highlights that our backbone not only achieves higher asymptotic performance but also generalizes better to novel obstacle geometries.

Across both unseen settings, *SSD-Mamba2* consistently outperforms strong baselines. On rugged terrain, it prioritizes progress while maintaining competitive safety; in dynamic obstacle settings, it achieves both higher returns and fewer collisions. Together with the in-distribution experiments and mechanism visualizations, these findings demonstrate that se-

TABLE V: Zero-shot performance on *Rugged Terrain with Thin Obstacles & Goals*. Mean \pm std over 10 runs.

Method	Return	Collision Times	Distance Moved (m)
Proprio-Only	70.24 ± 41.11	735.37 ± 120.63	3.44 ± 1.26
Transformer Vision-Only	52.29 ± 54.78	—	2.34 ± 1.48
Mamba2 Vision-Only	12.07 ± 62.11	—	1.68 ± 1.65
Transformer Proprio-Vision	432.32 ± 182.28	560.47 ± 152.65	9.22 ± 3.01
SSD-Mamba2 (Ours)	601.62 ± 289.57	638.93 ± 118.38	11.31 ± 4.94

TABLE VI: Zero-shot performance on *Sphere Obstacles & Goals*. Mean \pm std over 10 runs.

Method	Return	Collision Times	Distance Moved (m)
Proprio-Only	85.48 ± 92.37	482.37 ± 136.02	5.50 ± 2.36
Transformer Vision-Only	41.02 ± 36.82	—	2.15 ± 0.91
Mamba Vision-Only	82.74 ± 45.02	—	3.87 ± 0.84
Transformer Proprio-Vision	467.56 ± 230.68	163.17 ± 77.44	10.26 ± 4.54
SSD-Mamba2 (Ours)	608.47 ± 344.02	158.77 ± 117.62	12.24 ± 7.04

lective state-space fusion enables policies that are robust, foresighted, and transferable beyond their training environments.

V. CONCLUSION

This work introduced *SSD-Mamba2*, a vision-driven cross-modal reinforcement learning framework for motion control. By encoding proprioceptive states with an MLP, patchifying depth images with a lightweight CNN, and fusing them through stacked SSD-Mamba2 layers, the method leverages state-space duality to achieve efficient long-horizon modeling with near-linear complexity. Coupled with PPO and a compact reward design under domain randomization and curriculum scheduling, the framework enables stable and scalable end-to-end training.

Extensive experiments demonstrated that *SSD-Mamba2* consistently outperforms proprioception-only, vision-only, and Transformer-based baselines in terms of return, safety (fewer collisions and falls), and distance traveled. Learning-curve and stability analyses further confirmed its superior convergence speed, sample efficiency, and robustness. Ablation studies highlighted the critical role of cross-modal fusion and validated the effectiveness of *SSD-Mamba2* as a fusion backbone for safety-critical locomotion.

While this study focused on simulated environments, future work will extend to hardware deployment, evaluating sim-to-real transfer, latency, and safety in real-world quadrupedal platforms. Beyond locomotion, the proposed approach may also benefit broader motion-control domains such as mobile navigation and human–robot interaction, where efficient fusion of multimodal signals is crucial.

REFERENCES

- [1] S. Imambi, K. B. Prakash, and G. Kanagachidambaresan, “Pytorch,” in *Programming with TensorFlow: solution for edge computing applications*. Springer, 2021, pp. 87–104.
- [2] J. Carpentier and P.-B. Wieber, “Recent progress in legged robots locomotion control,” *Current Robotics Reports*, vol. 2, no. 3, pp. 231–238, 2021.
- [3] Z. Xie, X. Da, B. Babich, A. Garg, and M. v. de Panne, “Glide: Generalizable quadrupedal locomotion in diverse environments with a centroidal model,” in *International workshop on the algorithmic foundations of robotics*. Springer, 2022, pp. 523–539.
- [4] X. Han, S. Chen, Z. Fu, Z. Feng, L. Fan, D. An, C. Wang, L. Guo, W. Meng, X. Zhang, *et al.*, “Multimodal fusion and vision-language models: A survey for robot vision,” *arXiv preprint arXiv:2504.02477*, 2025.
- [5] K. Li, W. Gao, and S. Zhang, “Rapid learning of natural gaits for quadrupedal locomotion and skill reuse in downstream tasks,” in *2024 IEEE International Conference on Robotics and Biomimetics (ROBIO)*. IEEE, 2024, pp. 2330–2336.
- [6] D. Jain, A. Iscen, and K. Caluwaerts, “Hierarchical reinforcement learning for quadruped locomotion,” in *2019 IEEE/RSJ international conference on intelligent robots and systems (IROS)*. IEEE, 2019, pp. 7551–7557.
- [7] R. Yang, M. Zhang, N. Hansen, H. Xu, and X. Wang, “Learning vision-guided quadrupedal locomotion end-to-end with cross-modal transformers,” *arXiv preprint arXiv:2107.03996*, 2021.
- [8] T. Dao and A. Gu, “Transformers are ssms: Generalized models and efficient algorithms through structured state space duality,” 2024. [Online]. Available: <https://arxiv.org/abs/2405.21060>
- [9] I. Tolstikhin, N. Houlsby, A. Kolesnikov, L. Beyer, X. Zhai, T. Unterthiner, J. Yung, A. Steiner, D. Keysers, J. Uszkoreit, M. Lucic, and A. Dosovitskiy, “Mlp-mixer: An all-mlp architecture for vision,” 2021. [Online]. Available: <https://arxiv.org/abs/2105.01601>
- [10] K. O’Shea and R. Nash, “An introduction to convolutional neural networks,” 2015. [Online]. Available: <https://arxiv.org/abs/1511.08458>
- [11] J. Schulman, F. Wolski, P. Dhariwal, A. Radford, and O. Klimov, “Proximal policy optimization algorithms,” *arXiv preprint arXiv:1707.06347*, 2017.
- [12] R. Yang, M. Zhang, N. Hansen, H. Xu, and X. Wang, “Learning vision-guided quadrupedal locomotion end-to-end with cross-modal transformers,” in *International Conference on Learning Representations*, 2022. [Online]. Available: <https://openreview.net/forum?id=nhnJ3oo6AB>
- [13] H. Miura and I. Shimoyama, “Dynamic walk of a biped,” *The International Journal of Robotics Research*, vol. 3, no. 2, pp. 60–74, 1984.
- [14] Z. G. Liu and X. F. Ding, “Planning and simulation of the rule-based trotting gait of a bionic quadruped robot,” *Advanced Materials Research*, vol. 971, pp. 624–628, 2014.
- [15] Y. Habu, Y. Yamada, S. Fukui, and Y. Fukuoka, “A simple rule for quadrupedal gait transition proposed by a simulated muscle-driven quadruped model with two-level cpgs,” in *2018 IEEE International Conference on robotics and biomimetics (ROBIO)*. IEEE, 2018, pp. 2075–2081.
- [16] G. Bledt, M. J. Powell, B. Katz, J. Di Carlo, P. M. Wensing, and S. Kim, “Mit cheetah 3: Design and control of a robust, dynamic quadruped robot,” in *2018 IEEE/RSJ International Conference on Intelligent Robots and Systems (IROS)*. IEEE, 2018, pp. 2245–2252.
- [17] R. Grandia, F. Farshidian, R. Ranftl, and M. Hutter, “Feedback mpc for torque-controlled legged robots,” in *2019 IEEE/RSJ International Conference on Intelligent Robots and Systems (IROS)*. IEEE, 2019, pp. 4730–4737.
- [18] Q. Yao, J. Wang, D. Wang, S. Yang, H. Zhang, Y. Wang, and Z. Wu, “Hierarchical terrain-aware control for quadrupedal locomotion by combining deep reinforcement learning and optimal control,” in *2021 IEEE/RSJ International Conference on Intelligent Robots and Systems (IROS)*. IEEE, 2021, pp. 1–8.

IEEE/RSJ International Conference on Intelligent Robots and Systems (IROS), 2021, pp. 4546–4551.

[19] L. Amatucci, G. Turrisi, A. Bratta, V. Barasuol, and C. Semini, “Accelerating model predictive control for legged robots through distributed optimization,” in *2024 IEEE/RSJ International Conference on Intelligent Robots and Systems (IROS)*. IEEE, 2024, pp. 12 734–12 741.

[20] M. Elbaid, G. Turrisi, L. Rapetti, G. Romualdi, S. Dafarra, T. Kawakami, T. Chaki, T. Yoshihike, C. Semini, and D. Pucci, “Adaptive non-linear centroidal mpc with stability guarantees for robust locomotion of legged robots,” *IEEE Robotics and Automation Letters*, 2025.

[21] J. Di Carlo, P. M. Wensing, B. Katz, G. Bledt, and S. Kim, “Dynamic locomotion in the mit cheetah 3 through convex model-predictive control,” in *2018 IEEE/RSJ international conference on intelligent robots and systems (IROS)*. IEEE, 2018, pp. 1–9.

[22] Y. Ding, A. Pandala, and H.-W. Park, “Real-time model predictive control for versatile dynamic motions in quadrupedal robots,” in *2019 International Conference on Robotics and Automation (ICRA)*. IEEE, 2019, pp. 8484–8490.

[23] J. Carius, R. Ranftl, V. Koltun, and M. Hutter, “Trajectory optimization for legged robots with slipping motions,” *IEEE Robotics and Automation Letters*, vol. 4, no. 3, pp. 3013–3020, 2019.

[24] Z. Li, X. Cheng, X. B. Peng, P. Abbeel, S. Levine, G. Berseth, and K. Sreenath, “Reinforcement learning for robust parameterized locomotion control of bipedal robots,” in *2021 IEEE International Conference on Robotics and Automation (ICRA)*. IEEE, 2021, pp. 2811–2817.

[25] G. B. Margolis, G. Yang, K. Paigwar, T. Chen, and P. Agrawal, “Rapid locomotion via reinforcement learning,” *The International Journal of Robotics Research*, vol. 43, no. 4, pp. 572–587, 2024.

[26] R. Bussola, M. Focchi, G. Turrisi, C. Semini, and L. Palopoli, “Guided reinforcement learning for omnidirectional 3d jumping in quadruped robots,” *arXiv preprint arXiv:2507.16481*, 2025.

[27] J. Tan, T. Zhang, E. Coumans, A. Iscen, Y. Bai, D. Hafner, S. Bohez, and V. Vanhoucke, “Sim-to-real: Learning agile locomotion for quadruped robots,” *arXiv preprint arXiv:1804.10332*, 2018.

[28] J. Hwangbo, J. Lee, A. Dosovitskiy, D. Bellicoso, V. Tsounis, V. Koltun, and M. Hutter, “Learning agile and dynamic motor skills for legged robots,” *Science Robotics*, vol. 4, no. 26, p. eaau5872, 2019.

[29] A. Kumar, Z. Fu, D. Pathak, and J. Malik, “Rma: Rapid motor adaptation for legged robots,” *arXiv preprint arXiv:2107.04034*, 2021.

[30] J. Lee, J. Hwangbo, L. Wellhausen, V. Koltun, and M. Hutter, “Learning quadrupedal locomotion over challenging terrain,” *Science robotics*, vol. 5, no. 47, p. eabc5986, 2020.

[31] Z. Xie, X. Da, M. Van de Panne, B. Babich, and A. Garg, “Dynamics randomization revisited: A case study for quadrupedal locomotion,” in *2021 IEEE International Conference on Robotics and Automation (ICRA)*. IEEE, 2021, pp. 4955–4961.

[32] S. Fahmi, V. Barasuol, D. Esteban, O. Villarreal, and C. Semini, “Vital: Vision-based terrain-aware locomotion for legged robots,” *IEEE Transactions on Robotics*, vol. 39, no. 2, pp. 885–904, 2022.

[33] B. Singh, R. Kumar, and V. P. Singh, “Reinforcement learning in robotic applications: a comprehensive survey,” *Artificial Intelligence Review*, vol. 55, no. 2, pp. 945–990, 2022.

[34] F. Xiao, T. Chen, and Y. Li, “Egocentric visual locomotion in a quadruped robot,” in *Proceedings of the 2024 8th International Conference on Electronic Information Technology and Computer Engineering*, 2024, pp. 172–177.

[35] H. Lai, J. Cao, J. Xu, H. Wu, Y. Lin, T. Kong, Y. Yu, and W. Zhang, “World model-based perception for visual legged locomotion,” *arXiv preprint arXiv:2409.16784*, 2024.

[36] Y. Wang and G. Tao, “Locomamba: Vision-driven locomotion via end-to-end deep reinforcement learning with mamba,” 2025. [Online]. Available: <https://arxiv.org/abs/2508.11849>

[37] A. Gu, K. Goel, and C. Ré, “Efficiently modeling long sequences with structured state spaces,” *arXiv preprint arXiv:2111.00396*, 2021.

[38] A. Gu and T. Dao, “Mamba: Linear-time sequence modeling with selective state spaces,” *arXiv preprint arXiv:2312.00752*, 2023.

[39] Y. Li, Y. Xing, X. Lan, X. Li, H. Chen, and D. Jiang, “Alignmamba: Enhancing multimodal mamba with local and global cross-modal alignment,” in *Proceedings of the Computer Vision and Pattern Recognition Conference*, 2025, pp. 24 774–24 784.

[40] X. Xie, Y. Cui, T. Tan, X. Zheng, and Z. Yu, “Fusionmamba: Dynamic feature enhancement for multimodal image fusion with mamba,” *Visual Intelligence*, vol. 2, no. 1, p. 37, 2024.

[41] J. Ye, J. Zhang, and H. Shan, “Depmamba: Progressive fusion mamba for multimodal depression detection,” in *ICASSP 2025-2025 IEEE International Conference on Acoustics, Speech and Signal Processing (ICASSP)*. IEEE, 2025, pp. 1–5.

[42] N. Tan, “Computation of stabilizing pi-pd controllers,” *International Journal of Control, Automation and Systems*, vol. 7, no. 2, pp. 175–184, 2009.

[43] E. Coumans and Y. Bai, “Pybullet quickstart guide,” *ed: PyBullet Quickstart Guide. https://docs.google.com/document/u/1/d*, 2021.

[44] B. Mehta, M. Diaz, F. Golemo, C. J. Pal, and L. Paull, “Active domain randomization,” in *Conference on Robot Learning*. PMLR, 2020, pp. 1162–1176.

[45] X. Wang, Y. Chen, and W. Zhu, “A survey on curriculum learning,” *IEEE transactions on pattern analysis and machine intelligence*, vol. 44, no. 9, pp. 4555–4576, 2021.